Applied Acoustics 246 (2026) 111222

Contents lists available at ScienceDirect

Applied Acoustics

journal homepage: www.elsevier.com/locate/apacoust

Unsupervised seabed habitat change detection with multibeam backscatter data using a constrained Gaussian mixture model

Qian Bai [a,*], Alireza Amiri-Simkooei [a], Sebastiaan Mestdagh [b], Dick G. Simons [a], Mirjam Snellen [a]

[a] Faculty of Aerospace Engineering, Delft University of Technology, Delft, the Netherlands
[b] Department of Ecosystems and Sediment Dynamics, Deltares, Delft, the Netherlands

HIGHLIGHTS

- Unsupervised seabed change detection via backscatter differences across surveys and relative calibration on a reference area.
- Unchanged seabed is modeled as a zero-mean Gaussian, with its variance constrained by reference-area backscatter uncertainty.
- Backscatter differences from incident angles between 40° and 60° present the largest ability of seabed change detection.
- Detected changes align with the sediment movement and a reduction in sand mason worms between the repeated surveys.

ARTICLE INFO

Keywords:
Multibeam echosounder
Change detection
Unsupervised
Seabed habitat
North sea

ABSTRACT

Seabed backscatter data acquired by the multibeam echosounder (MBES) have been identified as a valuable indicator of sediment properties and benthic community characteristics. However, developing robust change detection models with MBES backscatter remains challenging due to the high costs and limited spatial coverage of seabed ground truth data. Lack of absolute backscatter calibration also hinders the comparison between repeated MBES measurements. To mitigate these issues, we propose an unsupervised method to detect seabed changes by fitting a Gaussian Mixture Model to the backscatter difference between two datasets. A relative calibration is conducted based on a stable reference area to eliminate the impact of possible drifts in echosounder characteristics on the backscatter difference. We then model the unchanged class as a zero-mean Gaussian distribution, with its variance constrained by the backscatter uncertainty estimated from the reference area. By processing each incident angle individually, the angular range with the greatest ability for seabed change detection can also be investigated. We demonstrate the effectiveness of the proposed method through two case studies in the Dutch North Sea. The detected changes reveal seasonal and temporal variations in benthic communities, such as sand mason worms, and are consistent with the sediment movement in one of the study areas. This research highlights the value of MBES backscatter data for seabed change detection and provides a cost-effective solution for seabed habitat monitoring with acoustic measurements.

1. Introduction

Regular seabed monitoring is important for preserving and managing marine habitats [1–3]. Traditional ecological monitoring techniques, such as box coring and trawling, provide precise but spatially sparse seabed information. These techniques also disturb the benthic habitats, which restricts the locations and frequency of sampling [4]. By contrast, acoustic techniques, especially the multibeam echosounder (MBES), offer a non-destructive and efficient approach for seabed characterization. Installed on a vessel platform, MBES emits sound waves in a wide swath perpendicular to the sailing direction and collects the backscattered signals. The beamsteering technique can distinguish signals backscattered from different directions, resulting in measurements for bathymetry and seabed backscatter intensity across various geolocations [5].

Previous research has successfully employed MBES backscatter data to characterize sea bottom properties, such as the sediment grain size [6–8], the occurrence of marine benthos [9–13], and manmade structures [14,15]. Considering the ability of MBES for continuous and

* Corresponding author.
Email address: q.bai@tudelft.nl (Q. Bai).

https://doi.org/10.1016/j.apacoust.2026.111222
Received 12 May 2025; Received in revised form 1 January 2026; Accepted 1 January 2026
Available online 7 January 2026

broad-scale seabed mapping across various applications, repeated MBES surveys provide a promising solution for inspecting seabed changes over time [16]. Such advances highlight MBES as an important tool for monitoring and managing dynamic marine environments.

Generally speaking, change detection from multi-temporal remote sensing datasets has been a prominent research topic for decades [17]. Given the ground truth data, supervised methods including machine learning and deep learning approaches can be applied for change detection. One common supervised approach is the post-classification comparison, where two classified images are compared to generate a change matrix [18]. Similarly, Montereale-Gavazzi et al. [19] classified MBES data from six surveys using the Random Forest algorithm. In their study, comparisons of the classification maps revealed temporal changes in three seabed sediment types over a ten-year period. However, collecting ground truth data for environmental monitoring can be time-consuming and labor-intensive. In seabed mapping applications, the aquatic environment poses additional challenges for accessing the seabed and achieving ground truth samples with accurate localization [20]. In this regard, unsupervised change detection methods, which minimize the dependence on ground truth data, offer a valuable alternative for monitoring dynamic seafloor environments.

Unsupervised classification methods have also been employed in the post-classification comparison to detect seabed changes. For example, Gaida et al. [20] identified changes in underwater coastal nourishment materials from eight surveys by comparing the unsupervised Bayesian classification [21] results of the MBES backscatter data. To avoid misinterpreting the possible drifts in sonar system characteristics as the seabed changes, they classified the backscatter data from each survey separately. However, some overall changes in the study area might be overlooked when comparing patterns of the separately classified maps without ground truth data from each survey. Feature differencing, on the other hand, offers a more straightforward approach for comparing datasets acquired at different times. Analyzing the difference between two co-registered datasets is a widely adopted method for change detection [22]. Seabed monitoring using the bathymetric differences from repeated surveys has also been investigated [23]. Seabed change detection using the MBES backscatter differences, however, remains an area that requires further research.

Analyzing the backscatter differences among distinct surveys poses several challenges mainly due to the absence of absolute backscatter calibration. Some sonar parameters such as directivity patterns can be proprietary and hence unavailable to users. Moreover, the aging of MBES components or changes in the seawater environment can also affect the hardware sensitivity. In addition, the angular variation of the backscatter intensity introduces across-track inconsistencies in the backscatter data, which further complicates the process of feature differencing.

Building on the aforementioned gaps and challenges, this research aims to identify seabed habitat changes in an unsupervised manner by analyzing the backscatter differences between two MBES datasets. To make the two backscatter datasets comparable, we conduct a relative calibration using a stable reference area, which has been indicated as an effective approach for making the temporal backscatter data intrinsically relative [24,25]. Following this, seabed changes are analyzed for each incident angle separately by clustering the backscatter differences using a Gaussian Mixture Model (GMM). Gaussian distribution is a widely used assumption for change detection [26]. Regarding the MBES backscatter data, statistical properties of the beam-averaged backscatter strength also allow the use of Gaussian distributions. To ensure the separation between unchanged and changed seabed areas, constraints are introduced to the GMM: the unchanged cluster is modeled as a zero-mean Gaussian, where its variance is initialized by the uncertainty estimated from the backscatter data within the reference area.

We applied the proposed change detection method to MBES datasets acquired in two study areas in the Dutch North Sea. We used backscatter data at 300 kHz, a frequency commonly employed for high-resolution seafloor mapping in shallow coastal waters. Our detection results align with the observed geomorphological changes in seabed sediments and suggest a potential reduction in living benthos such as *Lanice conchilega* (sand mason worms) between two measurement periods, showing that the proposed method can be a cost-effective solution for monitoring the benthic habitat. The constrained GMM method also reveals the difference in change detection performance regarding different incident angles, facilitating the design of future surveys for acoustic seabed mapping.

2. Methods

The workflow of our seabed change detection method can be divided into three steps: data preprocessing, backscatter difference preparation, and change detection using the constrained GMM (see Fig. 1).

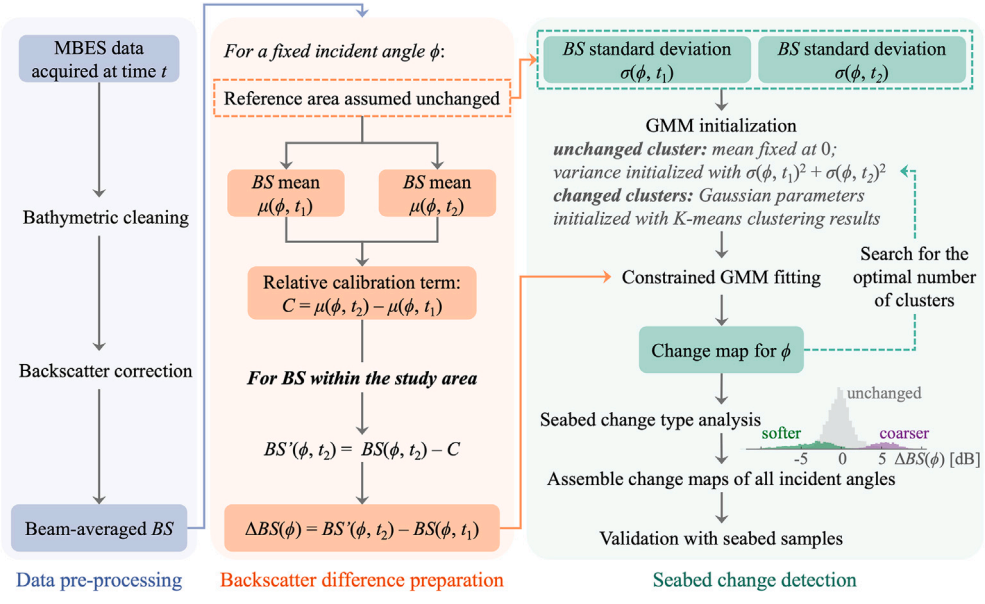

Fig. 1. Workflow for seabed change detection using MBES backscatter measurements from two surveys.

2.1. Data preprocessing

We remove the bathymetric outliers through spline filtering and use the remaining soundings for backscatter data analysis. Apart from geophysical and biological seabed properties, the echo level received by an MBES is affected by many factors, including acoustic frequency, incident angle, water column properties, seabed geomorphology, and certain sonar settings. To accurately make use of MBES backscatter data for seabed habitat characterization, it is essential to account for these factors.

With a fixed acoustic frequency, the backscatter strength (BS) [dB per m^2 at 1 m] exclusively representing the sea bottom material properties can be determined according to the sonar equation [5]:

$$BS(\phi) = EL + 2TL - SL - G - SH - BP_T(\theta_T) - BP_R(\theta_R) - 10\log A, \quad (1)$$

where ϕ is the actual incident angle relative to the seabed slope. EL indicates the echo level [dB] backscattered to the MBES. SL is the source level [dB re 1 μPa at 1 m]. BP_T and BP_R are the directivity patterns at the transmission angle θ_T and receiving angle θ_R relative to the sonar axis. G and SH refer to the receiver gain [dB] and transducer sensitivity [dB re 1 V/μPa], respectively. In addition to the above sonar parameters, TL in Eq. (1) accounts for the one-way transmission loss through the water column, consisting of the geometrical spreading and seawater absorption:

$$TL = 20\log R + \alpha R, \quad (2)$$

with R being the one-way travel distance of the acoustic signal from the sonar to the seabed and α being the absorption coefficient [dB/m].

In addition, the insonified beam footprint A is considered to derive the backscatter strength in the unit area. A is determined as the smaller value between the beam-limited regime A_b and pulse-limited regime A_p [27], which are

$$A_b = R^2 \Omega_{al} \Omega_{ac}, \quad (3)$$

and

$$A_p = \Omega_{al} R \frac{c\tau_e}{2\sin(\phi_{fl} - \epsilon_{ac})\cos(\epsilon_{al})}, \quad (4)$$

where Ω_{al} and Ω_{ac} are the along- and across-track beam opening angles, respectively. c refers to the sound velocity [m/s] and τ_e is the effective pulse length [s]. Moreover, ϕ_{fl} is the nominal incident angle relative to a horizontal and flat seabed. ϵ_{ac} and ϵ_{al} indicate the across- and along-track seabed slope [radians], respectively, accounting for the impact of seabed geomorphology on BS. We estimate ϵ_{ac} and ϵ_{al} using a 2D finite difference method, with a moving window of 60 pings on the bathymetry data [28].

With the seabed slopes ϵ_{ac} and ϵ_{al}, the actual incident angle ϕ can then be derived as

$$\phi = \arccos\left(\frac{\cos\phi_{fl} + \epsilon_{ac}\sin\phi_{fl}}{\sqrt{1 + \epsilon_{al}^2 + \epsilon_{ac}^2}} \right). \quad (5)$$

Achieving the absolute backscatter correction described in Eq. (1) is challenging due to the absence of knowledge of sonar parameters such as SH and the directivity patterns. For MBES backscatter measurements of a single survey, these unknown parameters can be considered as fixed values. By properly handling other factors, we can still achieve uncalibrated BS representing the variation in seabed properties. However, comparing or combining backscatter data across multiple surveys will require either absolute or relative sonar calibration to account for the impact of possible changes in the system characteristics across different surveys.

2.2. Backscatter difference preparation

The difference in BS between two MBES datasets collected at time t_1 and t_2 for the same study area is the input to our seabed change detection method. Considering the angular dependence of BS, we analyze BS for each incident angle ϕ separately. To avoid including the change in sonar characteristics in the backscatter difference, $\Delta BS(\phi)$, we conduct a relative calibration on $BS(\phi, t_2)$ using a reference area.

2.2.1. Reference area selection

Ideally, the reference area should remain sufficiently stable over time in terms of bathymetry and geomorphology, as validated by successive surveys [25,29]. The reference area selection follows several criteria. First, the area should be flat and stable in bathymetry over time. In principle, the bathymetric change of the area from t_1 to t_2 should remain within the uncertainty of MBES depth measurements. The flatness can be examined by the seabed slope estimations, and the occurrence of simple unidirectional patterns is acceptable [25]. In addition, the area should exhibit homogeneity in backscatter data at both t_1 and t_2.

Since such an independent reference area was inaccessible during our surveys, we selected a homogeneous and stable region within our study area (see Section 4.2). For the selected area fulfilling these requirements, we further validated its stability over time by assessing the consistency of nearby bottom samples taken at t_1 and t_2, considering their median grain size, benthos composition, and presence of dead shells.

2.2.2. Relative calibration

After selecting the reference area, the relative calibration of BS from different surveys is straightforward (Fig. 1). For each incident angle ϕ, we compute the average BS within the reference area from t_1 and t_2, denoted as $\mu(\phi, t_1)$ and $\mu(\phi, t_2)$. The relative calibration term C is then determined as

$$C(\phi) = \mu(\phi, t_2) - \mu(\phi, t_1). \quad (6)$$

If $BS(\phi, t_2)$ represents any BS value in the study area for ϕ at t_2, the relative calibration can be achieved by

$$BS'(\phi, t_2) = BS(\phi, t_2) - C(\phi), \quad (7)$$

which accounts for the MBES systematic difference between t_1 and t_2. Following this, we achieve the corrected backscatter difference as input to the change detection algorithm through:

$$\Delta BS(\phi) = BS'(\phi, t_2) - BS(\phi, t_1). \quad (8)$$

2.3. Seabed change detection: Constrained GMM

We propose to detect seabed changes by clustering $\Delta BS(\phi)$ using the GMM, since the nature of the beam-averaged backscatter strength allows us to model $\Delta BS(\phi)$ as Gaussian distributions.

Given the ping-by-ping emission of an MBES, $BS(\phi)$ can be treated as a random variable affected by the seabed geoacoustic properties. Within each beam, $BS(\phi)$ results from averaging over the intensities of several independent scatter pixels, which correspond to the ensonified footprints of each pulse. According to the central limit theorem, when a sufficient number of scatter pixels are present, $BS(\phi)$ from a single seabed type follows a Gaussian distribution [21].

Therefore, given a fixed incident angle ϕ, the overall probability density function (PDF) of BS at time t_1 can be represented by a Gaussian mixture as

$$f_1(x) = \sum_{i=1}^{m_1} \frac{w_{1,i}}{\sqrt{2\pi\sigma_{1,i}^2}} \exp\left[-\frac{(x - \mu_{1,i})^2}{2\sigma_{1,i}^2} \right], \quad (9)$$

where x is one observation from $BS(\phi, t_1)$, m_1 is the total number of seabed types present at time t_1, and $w_{1,i}$, $\mu_{1,i}$, and $\sigma_{1,i}$ are the

weight coefficient, mean, and standard deviation of the i-th seabed type, respectively.

Similarly, for the same study area and ϕ, the PDF of BS at time t_2 can be written as

$$f_2(x) = \sum_{j=1}^{m_2} \frac{w_{2,j}}{\sqrt{2\pi\sigma_{2,j}^2}} \exp\left[-\frac{(x-\mu_{2,j})^2}{2\sigma_{2,j}^2}\right]. \tag{10}$$

For seabed change detection, assuming that MBES measurements at t_1 and t_2 are independent, the PDF of $\Delta BS(\phi) = BS(\phi, t_2) - BS(\phi, t_1)$ can then be derived as

$$f_\Delta(x) = \sum_{k=1}^{m_1 m_2} \frac{\tilde{w}_{\Delta,k}}{\sqrt{2\pi\tilde{\sigma}_{\Delta,k}^2}} \exp\left[-\frac{(x-\tilde{\mu}_{\Delta,k})^2}{2\tilde{\sigma}_{\Delta,k}^2}\right]. \tag{11}$$

where $\tilde{w}_{\Delta,k} = w_{1,i} w_{2,j}$, $\tilde{\mu}_{\Delta,k} = \mu_{2,j} - \mu_{1,i}$, and $\tilde{\sigma}_{\Delta,k}^2 = \sigma_{1,i}^2 + \sigma_{2,j}^2$ for each pair (i, j) assuming independent measurement noise at t_1 and t_2. x becomes one value in $\Delta BS(\phi)$.

In theory, the difference between $f_2(x)$ and $f_1(x)$ yields $m_1 m_2$ components corresponding to all possible transitions between seabed types. In practice, only a subset of these components is physically meaningful since many transitions do not occur within the study area. Moreover, at each location, only a single type of bottom change can occur, which limits the number of relevant components. Thus, we approximate Eq. (11) by n components:

$$f_\Delta(x) = \sum_{k=1}^{n} \frac{w_{\Delta,k}}{\sqrt{2\pi\sigma_{\Delta,k}^2}} \exp\left[-\frac{(x-\mu_{\Delta,k})^2}{2\sigma_{\Delta,k}^2}\right], \tag{12}$$

in which the first component represents the unchanged seabed and components 2 to n represent different types of seabed changes. The weight coefficient $w_{\Delta,k}$, $k = 1, \ldots, n$, satisfies $\sum_{k=1}^{n} w_{\Delta,k} = 1$. $\mu_{\Delta,k}$ and $\sigma_{\Delta,k}$ are the mean and standard deviation of the k-th seabed change type, respectively. $w_{\Delta,k}$, $\mu_{\Delta,k}$, and $\sigma_{\Delta,k}$ are the unknown parameters to be optimized.

Regarding the unchanged cluster, several constraints can be added to its Gaussian distribution. After appropriate backscatter correction and relative calibration, the mean of the unchanged cluster, $\mu_{\Delta,1}$, can be assumed to be 0. Theoretically, its variance $\sigma_{\Delta,1}^2$ is calculated as

$$\sigma_{\Delta,1}^2 = \sigma_u^2(t_1) + \sigma_u^2(t_2), \tag{13}$$

with $\sigma_u^2(t_1)$ and $\sigma_u^2(t_2)$ the uncertainty of $BS(\phi)$ measurements from the two distinct surveys, respectively. Since the random fluctuation of BS is affected by the seabed types, it is difficult to determine $\sigma_u^2(t_1)$ and $\sigma_u^2(t_2)$ without prior knowledge of the study area. Nevertheless, we can still facilitate the search for $\sigma_{\Delta,1}$ using the pre-selected reference area.

Within the reference area, where the seabed is homogeneous, $BS(\phi)$ can be seen as repeated measurements of the same seabed type. Since the reference area remains stable over time and experiences no change measurable with an MBES between t_1 and t_2, we can estimate the variance of backscatter difference for this specific seabed type as

$$\sigma'^2_{\Delta,1} = \sigma_r^2(t_1) + \sigma_r^2(t_2), \tag{14}$$

with σ_r^2 the variance of $BS(\phi)$ from the reference area. We then use $\sigma'_{\Delta,1}$ to initialize $\sigma_{\Delta,1}$ during optimization.

Regarding the remaining unknown parameters, the weights w_k of different Gaussian components are initialized equally. In addition, $\mu_{\Delta,k}$ and $\sigma_{\Delta,k}$ of the changed clusters are initialized using the cluster mean and standard deviation from the K-Means clustering [30] results. The K-Means cluster whose mean is closest to zero is excluded from this. K-Means clustering minimizes within-cluster data variances and might help separate GMM clusters. Following this, the unknown parameters in Eq. (12) are estimated by the Expectation-Maximization (EM) optimization algorithm [31].

In our implementation, computations for the constrained GMM and the EM optimization were performed in Python using the package *PyTorch*, while K-Means clustering was realized via *scikit-learn* using the '*kmeans++*' initialization. Regarding acoustic datasets in this study, computations ran efficiently on a desktop equipped with an Intel Xeon E5-1620 v3 CPU and 16 GB RAM, showing that no specialized hardware was required.

2.4. Evaluation

We evaluate the proposed change detection from two aspects: clustering performance and comparison with ground truth.

The clustering performance is evaluated using the silhouette coefficient [32], which quantifies how compact and well-separated the clusters are in feature space. The silhouette coefficient ranges from -1 (poor clustering) to 1 (well-clustered) and allows a direct comparison of clustering quality across incident angles for a fixed number of clusters. In particular, higher silhouette values indicate that ΔBS at a given angle provides better separation between the seabed change types.

In addition, we assess whether a given number of Gaussian components adequately explains the data distribution by computing the Bayesian information criterion (BIC) as a measure of goodness of fit [33]. Lower BIC values indicate a better trade-off between model fit and complexity. The silhouette coefficient and BIC are jointly used to select the optimal number of clusters/change types (n in Eq. 12).

With the available ground truth bottom samples, we examine how predicted changes correspond to variations in sample properties such as sediment grain size and benthic community presence, thereby linking our change detection results to specific seabed conditions. For locations sampled during both survey times, we also compute the accuracy and F1-score for the binary 'changed' and 'unchanged' classification. The accuracy describes the proportion of correctly predicted samples, while the F1-score is calculated as

$$\mathrm{F1} = 2\frac{\mathrm{Precision} \times \mathrm{Recall}}{\mathrm{Precision} + \mathrm{Recall}}, \tag{15}$$

where Precision measures the proportion of predicted 'changed' locations that truly experienced changes, and recall is the proportion of actual 'changed' samples correctly identified as 'changed'. Both accuracy and F1-score range from 0 (worst) to 1 (best).

3. Study areas and datasets

3.1. Study areas

We conducted hydrographic surveys in a subtidal region north of the Wadden Sea islands in the North Sea (see Fig. 2), where intensive economic activities take place, including fishing, offshore wind energy generation, and installation of cables and pipelines on the seabed [34]. Regular monitoring in this region is therefore essential for achieving a sustainable use of the seabed environment.

Our surveys, conducted in summer 2021 and early spring 2024, covered two study areas: Borkumse Stenen (BoS) and a region between Ameland and Terschelling (AT). Area BoS is characterized by a bathymetric drop in the middle, with more heterogeneous water depths on the deeper eastern seabed. By contrast, Area AT contains gradual seabed slopes, with a deep central trough. Due to limitations in time and budget, the 2024 survey covered only half of the initial survey extent in each study area. In addition, a seasonal difference in the seawater temperature (≈10°C) can be noticed between surveys in the two years (see Table 1).

3.2. Acoustic datasets

During all surveys, we collected the acoustic data using the same pole-mounted MBES system, R2Sonic 2026, with an acoustic frequency of 300 kHz. The beam opening angle was set to 0.7°, with a nominal pulse length of 150 μs. Under the equiangular beam spacing mode,

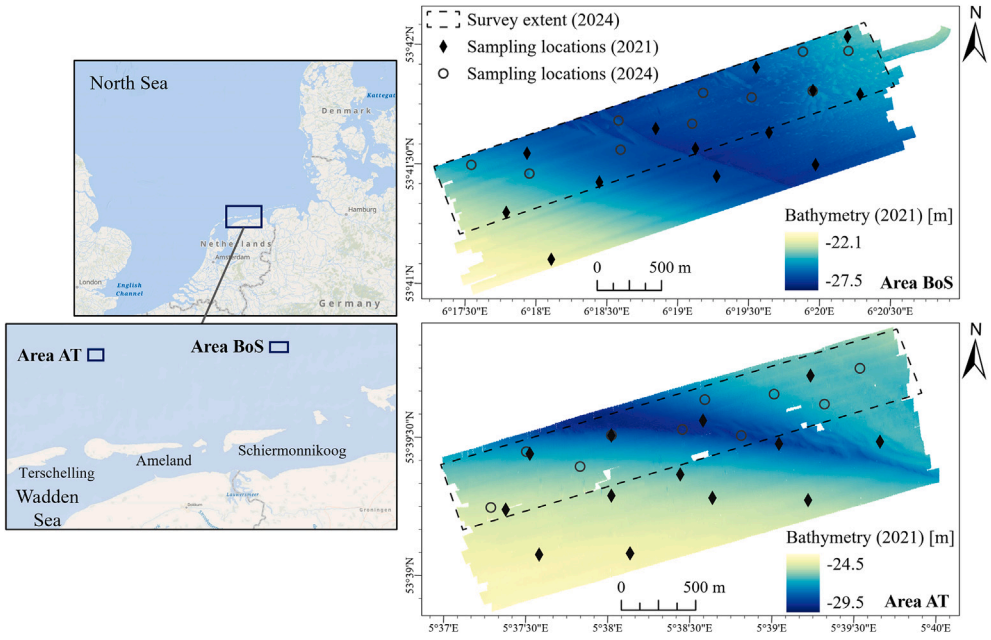

Fig. 2. Study areas. (Left) Location of the study areas in the North Sea. (Right) Bathymetry measured in 2021, displayed with the seabed sampling locations in 2021 and 2024.

Table 1
Survey time and seawater temperature of the study areas.

Study area	Survey time	Seawater temperature[1] [°C]
BoS	August 9–13, 2021	17.2±0.08
AT	July 12–16, 2021	16.7±0.06
BoS	March 13–14, 2024	7.3±0.14
AT	March 12–13, 2024	7.5±0.14

[1] Mean ± standard deviation for all water depths.

each ping contained 256 beams, covering a swath of 130°. In addition, adjacent track lines had approximately 50% overlap. To enable the comparison of $BS(\phi)$ between different surveys, we adopted the same sailing direction for the track lines in 2021 and 2024.

During the measurements, we used the hydrographic data acquisition software Qinsy to store the MBES bathymetry and backscatter data as database (.db) files. Conductivity, temperature, and depth (CTD) measurements were collected regularly to assist in accurate backscatter correction for sound absorption through the water column.

3.3. Seabed properties revealed by bottom samples

In 2021, 13 boxcore sampling locations were selected in Area BoS and AT for ground truthing. We used a cylindrical boxcore sampler with a surface area of 0.078 m^2. Pictures of the boxcore samples were taken onboard to provide a simple visual inspection. Macrofauna and sediment analyses were conducted later in the laboratory. In 2024, we selected 10 locations in BoS and AT for seabed sampling. Apart from boxcore samples, we took underwater videos above the seabed at each sampling location in 2024. Each video footage covered a transect of about 50 m, offering a qualitative assessment of the seabed conditions.

Sample analysis results from 2021 reveal a homogeneous seabed consisting of fine sand on the western side of Area BoS (Fig. 3). By contrast, the eastern seabed varied in sediment types from fine to coarse sand, with an abundant presence of *L. conchilega*, which are common in the subtidal sandy sediments of the North Sea [35]. *L. conchilega* are known for building tubes with sand grains and shell fragments. These tubes protrude outside the seabed surface, altering the seabed's geoacoustic properties to some extent [36]. Moreover, at location BC25, many clay chunks were found underneath the seabed surface. Area AT, on the other hand, had a narrower variation in sediment types (fine to medium sand). *L. conchilega* were also found in AT, especially in the coarser sediment of the trough.

In 2024, the spatial distribution of different sediment types in both study areas remained largely consistent with 2021. However, a new sediment type (msG) was identified in Area BoS from one boxcore sample taken in a region unsampled in 2021 (see N1 in Fig. 3). This region was found to have a high dead shell content in 2024. Clay chunks were also found at location N2, which is close to the location BC25 sampled in 2021. For other sampling locations in 2024 on the eastern seabed of BoS, the *L. conchilega* density was smaller compared to 2021. This is possibly due to the influence of seasonality on mortality and recruitment of the worms, considering that the life cycle of *L. conchilega* follows a seasonal pattern. Adult worms that survive the storms in autumn and winter spawn in spring, and juveniles usually settle on the seabed in late spring and summer [37,38]. In the central trough of Area AT, a lower density of *L. conchilega* and a higher percentage of dead shells were also found in spring 2024 compared to summer 2021.

4. Results and discussion

4.1. Relations between BS and seabed properties

To infer the type of seabed changes using $\Delta BS(\phi)$, relations between $BS(\phi)$ and seabed properties, such as the sediment grain size and benthos abundance, need to be examined first. In this way, we can link the increase or decrease in $BS(\phi)$ with certain seabed habitat changes. Fig. 4 presents the correlation analysis between seabed characteristics revealed by bottom samples and averaged BS from three angular ranges for our study areas. BS_1 from 0–25°, BS_2 from 25°–55°, and BS_3 from 55°–65° were obtained by averaging over 50 pings around each sampling location.

In general, BS_1, BS_2, and BS_3 are highly correlated, particularly in Area BoS surveyed in 2021. In 2021, *L. conchilega* in BoS was more abundant in coarse sediments (high Folk classes). The dead shell content also shows a moderate correlation with the Folk class. Moreover, the averaged BS across all three angular ranges correlates well with the

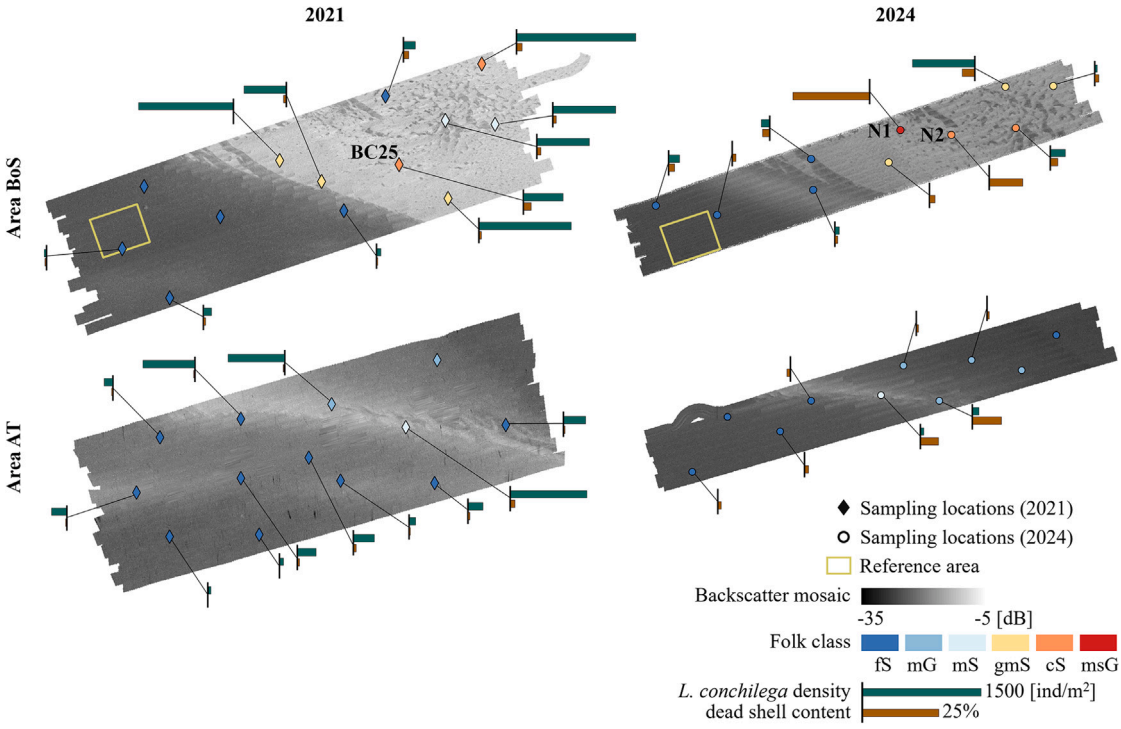

Fig. 3. Folk classes, *L. conchilega* (sand mason worm) density, and dead shell content for all boxcore samples collected in 2021 and 2024, displayed with the backscatter mosaic of each area. The backscatter mosaics were achieved using the software FMGT and only used for visual assessment. The 6 Folk classes correspond to an increase in the median grain size (fS: fine sand; mG: muddy gravel; mS: medium sand; gmS: gravelly muddy sand; cS: coarse sand; msG: muddy sandy gravel). *L. conchilega* density less than 20 [ind/m^2] or dead shell content smaller than 0.2% are not shown.

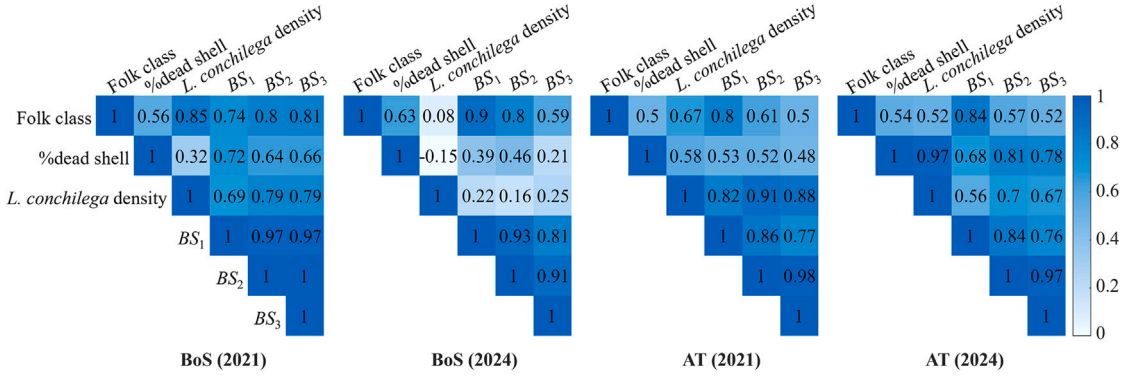

Fig. 4. Correlation matrix for each study area between the boxcore sample properties and mean BS from three angular ranges, with BS_1 from incident angles 0–25°, BS_2 from 25°–55°, and BS_3 from 55°–65°. Folk classes found in the study areas (fS–msG) are numbered from 1 to 6 when calculating the correlation coefficient.

Folk class. BS_2 and BS_3 exhibit moderate correlations with the dead shell content, and may be strongly affected by the *L. conchilega* density.

By contrast, BS_1, BS_2, and BS_3 show limited correlations with the *L. conchilega* density and dead shell content in the 2024 BoS survey. The relations between the Folk class and *L. conchilega* density also change significantly. Far fewer *L. conchilega* were found in most samples taken in 2024 than in 2021. In addition, bottom samples from locations N1 and N2 (Fig. 3) contained sediments with larger grain sizes and higher dead shell content than those collected in 2021. The differences in sampling locations might also contribute to the change in the correlation between the Folk class and *L. conchilega* occurrence. The two seabed properties might share a non-linear relationship, considering the preference of *L. conchilega* for sediments containing fine to medium sand [36]. Moreover, coarse materials from N1 and N2, such as dead shells, can exceed the acoustic wavelength and may no longer increase BS. Despite these variations, BS_1 and BS_2 remain highly correlated with the Folk class.

In Area AT, there are apparent differences among BS from the three angular ranges regarding their relations with the seabed properties. For both surveys in 2021 and 2024, BS_1 exhibits the strongest correlation with the Folk class. For 2021 data, BS_1, BS_2, and BS_3 show similar moderate correlations with the dead shell content and high correlations with the *L. conchilega* density. In 2024, bottom samples contained significantly fewer *L. conchilega* and generally higher dead shell content than in 2021. Compared to the results for 2021, correlations between BS and the *L. conchilega* density are weaker for AT surveyed in 2024, while BS_2 and BS_3 are highly correlated with the dead shell content.

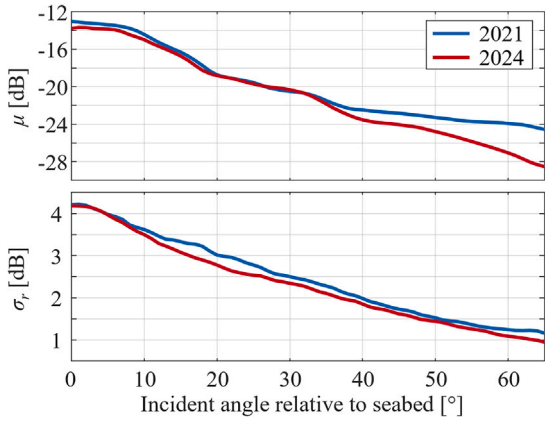

Fig. 5. Average half-swath angular response curves and standard deviations of BS from different incident angles within the reference area in 2021 and 2024. Incident angles with the same absolute value from the port and starboard side are considered identical, as the R2Sonic 2026 operates as a single-head system.

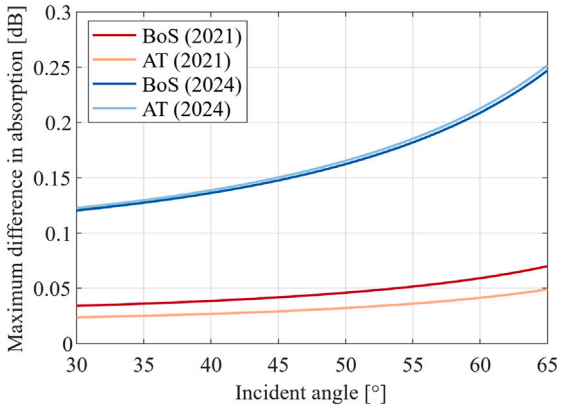

Fig. 6. Difference between seawater absorption in dB calculated using the minimum and maximum sound absorption coefficient acquired for a water depth of 25 m, displayed for incident angles 30°–65°.

4.2. Relative calibration results

The selected reference area (Fig. 3) covers approximately 300 × 360 m of seabed. Within this area, the average absolute bathymetric difference between the two surveys in 2021 and 2024 is 0.08 m. To assess whether this difference is consistent with expected measurement variability, we used the *A priori* Multibeam Uncertainty Simulation Tool (AMUST), which was developed to quantify the vertical uncertainty of MBES measurements [39,40]. Based on the echosounder specifications given in Section 3.2, the depth uncertainty is estimated to be in the range of 0.074–0.088 m at the 95% confidence level for water depths in Area BoS. Although part of the observed 0.08 m difference may be attributed to systematic errors, which are not accounted for in this assessment, the close agreement with the expected random uncertainty suggests that the seabed within the reference area has remained effectively stable between the two surveys. This is also confirmed by the average seabed slope, which remains consistent at 0.7° for both years. Backscatter mosaics further support this stability by a visual assessment of the seabed homogeneity within the reference area. Furthermore, boxcore samples next to the reference area demonstrate stability in the sediment type (fS) and very little presence of benthos, although there is a slight increase in dead shell content (≈0.8%) from 2021 to 2024.

The average backscatter angular response curves from the reference area, $\mu(2021)$ and $\mu(2024)$, show consistency between the 2021 and 2024 surveys for incident angles 20°–30° (see Fig. 5). However, there exists an increasing difference between $\mu(2021)$ and $\mu(2024)$ for incident angles larger than 30°, reaching approximately 4 dB for angles above 60°, which is consistent with the findings from a recent study on the instrumental temperature dependence of backscatter measurements [41]. Since the difference in sound absorption due to changes in seawater temperatures has been accounted for during the backscatter correction (Eq. 2), this effect might be attributed to the hardware sensitivity of the MBES system. In addition, we investigated the potential variation in the calculated two-way sound attenuation due to seawater absorption, by computing the difference between $2\alpha R$ in Eq. (2) using the minimum and maximum sound absorption coefficient (α) acquired for a water depth of 25 m. α was estimated based on *in-situ* CTD measurements during the survey period. Such difference does not exceed 0.3 dB from 30° to 65° (see Fig. 6), which is similar to values revealed by previous studies [20,41] and is not significant compared to the 4 dB difference observed between $\mu(2021)$ and $\mu(2024)$. Variations in this maximum difference of estimated seawater absorption across surveys can be attributed to seasonal differences in daily temperature fluctuations as well as different numbers of CTD measurements due to varying survey durations.

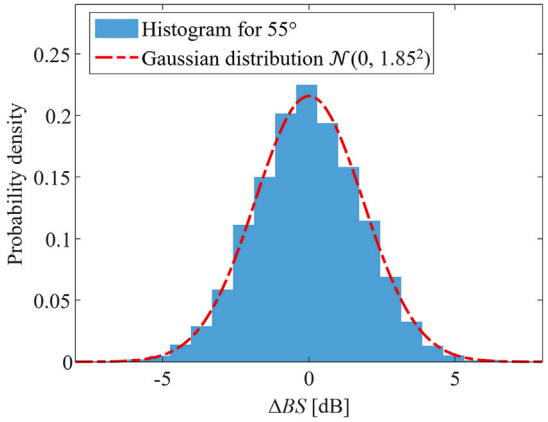

Fig. 7. Histogram of $\Delta BS(55°)$ within the reference area after relative calibration, displayed with the zero-mean Gaussian distribution $\mathcal{N}(0, \sigma_r(55°, 2021)^2 + \sigma_r(55°, 2024)^2) = \mathcal{N}(0, 1.85^2)$.

In this research, $\mu(2024)$ - $\mu(2021)$ was used as the relative calibration term for both Area BoS and AT, considering that the seawater temperature difference between the two study areas was small (Table 1). On the other hand, the standard deviations of BS within the reference area (σ_r) from the 2021 and 2024 surveys are generally consistent, with a decreasing trend as the incident angle increases (Fig. 5). This shows the stability regarding the uncertainty of MBES backscatter measurements from different surveys.

After applying the relative calibration, ΔBS within the reference area presents an example of backscatter difference of the unchanged seabed type. With the incident angle 55°, it is observed that the histogram of the resulting ΔBS can be approximated by a zero-mean Gaussian distribution, whose variance is calculated as $\sigma_r(2021)^2 + \sigma_r(2024)^2$ at 55° (Fig. 7). This is consistent with the assumption for constrained GMM.

4.3. Change detection: The optimal number of clusters

The silhouette coefficient and BIC quantitatively evaluate the clustering performance, facilitating the search for the optimal number of change types (n in Eq. 12). We compare the silhouette coefficients across five clustering methods: K-Means, GMM with random initialization (GMM-r), constrained GMM with random initialization (CGMM-r), GMM with Gaussian parameters initialized by K-Means clustering (GMM-k), and constrained GMM with K-Means initialization (CGMM-k). Since BIC

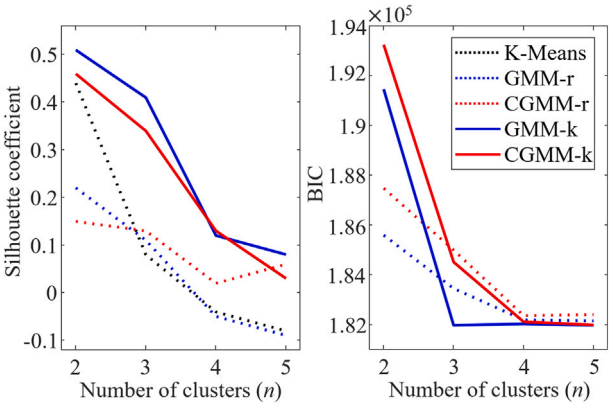

Fig. 8. Silhouette coefficients (Left) from five clustering methods and BIC values (Right) from GMM clustering methods for Area BoS, with the number of clusters ranging from 2 to 5. The presented metric value is an average value computed from the clustering results for incident angles 40°–60°. The clustering methods are: K-Means, GMM clustering with Gaussian parameters initialized randomly (GMM-r), GMM clustering with Gaussian parameters initialized by the K-Means clustering results (GMM-k), constrained GMM clustering with random initialization (CGMM-r), and constrained GMM clustering with K-Means initialization (CGMM-k).

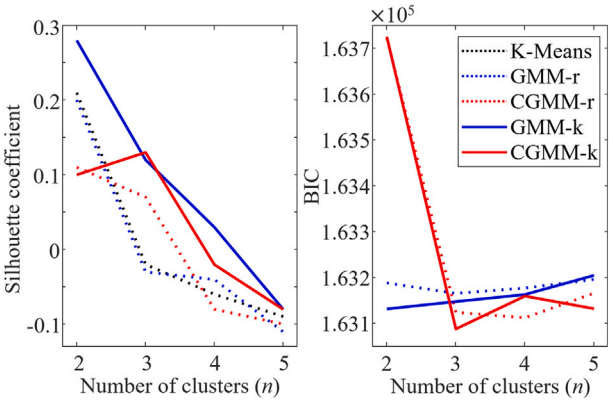

Fig. 9. Silhouette coefficients (Left) from five clustering methods and BIC values (Right) from GMM clustering methods for Area AT, with the number of clusters ranging from 2 to 5 and metric values averaged over 40°–60°.

is defined for parametric probabilistic models with an explicit likelihood function, we present BIC only for the GMM methods.

To compare the performance across different numbers of clusters, we computed the average metric values based on clustering results for incident angles between 40° and 60° (Fig. 8 and 9). This angular range was selected because ΔBS, for this angular range, exhibits the greatest capability to distinguish different seabed change types (see silhouette coefficient results in Section 4.4). Considering that this angular range is relatively narrow and contains a comparable number of valid BS values at each angle, the average BIC can also be representative of the overall model fit in this range.

For Area BoS, silhouette coefficients indicate that GMM-k and CGMM-k achieve better-separated clusters than the other methods, although results for $n \geq 4$ decrease significantly compared to two and three clusters (Fig. 8). With only two clusters, K-Means produces a silhouette coefficient comparable to GMM-k and CGMM-k, but its performance deteriorates significantly for more clusters. In general, GMM-based methods can further improve the K-Means clustering results by using them to initialize the Gaussian parameters. From GMM-r to GMM-k, the significant improvement in the silhouette coefficient also highlights the

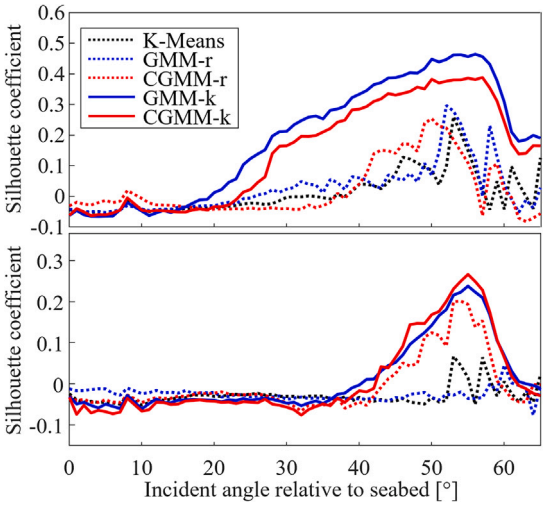

Fig. 10. Silhouette coefficient of 3 clusters for all incident angles for Area (Top) BoS and (Bottom) AT. Comparisons among five clustering methods are presented.

effectiveness of K-Means initialization in GMM optimization. GMM-r and CGMM-r fail to achieve satisfactory clustering results. However, the superior performance of CGMM-r for $n \geq 3$ compared to K-Means and GMM-r suggests the potential benefits of incorporating the proposed constraints. While silhouette coefficients show that $n = 2$ is optimal for Area BoS, BIC values suggest $n = 3$ for GMM-k and $n = 4$ for the other three GMM methods. Considering that GMM methods show little difference between silhouette coefficients for two and three clusters, but a significant decrease for four clusters, we chose 3 as the optimal number of clusters.

Clustering for Area AT generally yields lower silhouette coefficient values compared to results for BoS. There might be smaller differences among seabed change types in AT. For Area AT, GMM-k performs the best with two clusters (Fig. 9). CGMM-k achieves the best-separated clusters for $n = 3$, but shows similar silhouette coefficients to GMM-k and CGMM-r. By contrast, K-Means and GMM-r fail to effectively distinguish three clusters. With $n \geq 4$, silhouette coefficients of all methods are close to or smaller than zero, indicating poor clustering performance. Through a joint analysis of silhouette coefficients and BIC values, it is clear that $n = 3$ is an optimal choice for CGMM methods, while $n = 2$ might be suitable for the other methods. When visually assessing the cluster maps, it is found that the 'unchanged' detections from CGMM methods are scarcely present in the 2-cluster results, with most of the study area falling into a single 'changed' cluster. With three clusters in CGMM-r and CGMM-k, the spatial distribution of the 'unchanged' cluster remains consistent with the 2-cluster results, but an additional 'changed' cluster with a different spatial pattern is revealed. Notably, the two 'changed' clusters also coincide with the 2-cluster results from the other methods, which might indicate that most areas in AT experienced changes. Based on these observations, we ultimately chose three clusters for AT.

4.4. Change detection: Comparison among incident angles

With three clusters, all five methods achieve the best clustering performance for incident angles ranging from 40° to 60° (see Fig. 10). For Area BoS, all methods result in a silhouette coefficient close to zero for nadir beams up to 20°. Between 20° and 40°, K-Means, GMM-r, and CGMM-r have the silhouette coefficient still near zero, while CGMM-k and GMM-k can improve the clustering results significantly compared to the nadir beams. By contrast, for Area AT, most methods do not show clear separations for incident angles below 40°.

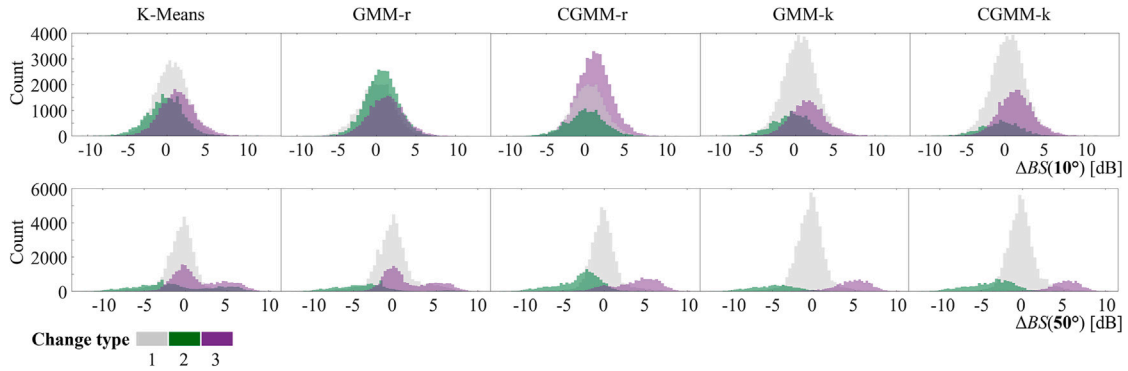

Fig. 11. Histogram of ΔBS for 10° and 50° regarding Area BoS, colored by the clustering results. Change type 1 can be interpreted as 'unchanged' for CGMM methods.

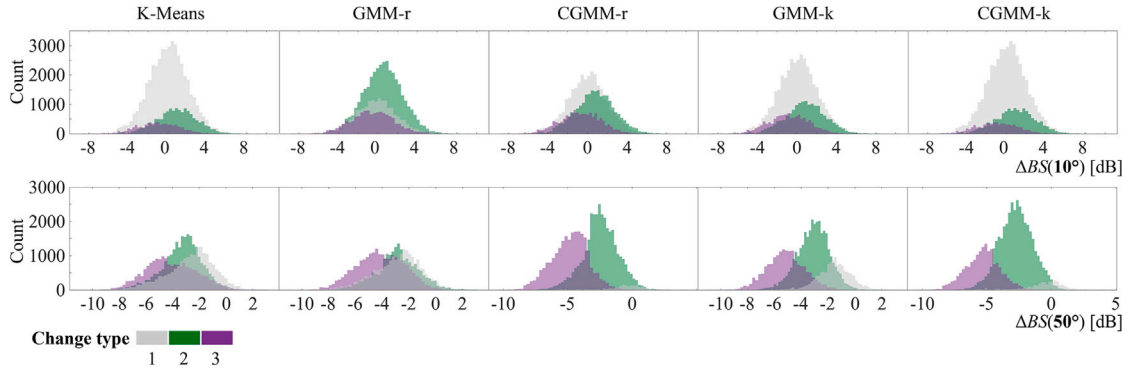

Fig. 12. Histogram of ΔBS for 10° and 50° regarding Area AT, colored by the clustering results. Change type 1 can be interpreted as 'unchanged' for CGMM methods.

Multiple factors contribute to the differences in clustering performances between nadir and oblique beams. Since BS from the nadir beams has a larger uncertainty (Fig. 5), distinguishing different seabed types becomes more challenging. Previous research [42] also suggested that a backscatter uncertainty of 2 dB is required to discriminate sediment types from fine to coarse sand, which is only met by the BS standard deviation within the 40°–60° range. In addition, seabed roughness and volume properties mainly affect BS at oblique angles [5]. Seabed changes related to these properties may not induce nadir ΔBS values exceeding the uncertainty of the backscatter measurements. Regarding GMM methods, BS in the nadir can violate the assumption of Gaussian distributions due to the insufficient number of scatter pixels within one beam [21], which can subsequently deteriorate the clustering performance.

Histograms of ΔBS at 10° and 50° provide a more detailed comparison of the clustering results for nadir and oblique angles (see Fig. 11 and 12). For both study areas, $\Delta BS(10°)$ varies around 0 dB, with substantial overlap among the three clusters. By contrast, $\Delta BS(50°)$ of Area BoS exhibits a much larger dispersion. Apart from one cluster centered at 0, cluster 2 with the negative backscatter difference is identified. Moreover, cluster 3 with $\Delta BS(50°)$ around 5 dB is clearly separated by GMM-k and CGMM-k (Fig. 11). In contrast with BoS, $\Delta BS(50°)$ of AT shows mostly negative values (Fig. 12). When using K-Means or GMM-r, clusters 1 and 2, which are closer to 0, overlap significantly. GMM-k improves cluster separation but does not center cluster 1 around 0 dB. The proposed CGMM methods, on the other hand, ensure that cluster 1 accurately represents the 'unchanged' seabed. Cluster 1 from CGMM-r and CGMM-k contains a very small number of data points, indicating that most of Area AT can be divided into the other two 'changed' clusters. For both study areas, CGMM-k can simultaneously enable the identification of the 'unchanged' seabed and maximize the separation among different clusters.

4.5. Seabed change type analysis

The 3-cluster change detection results from the CGMM methods distinguish the 'unchanged' seabed and two 'changed' clusters. Based on the relationship between BS and sample properties for our study areas (Fig. 4), we interpret the 'changed' cluster as 'coarser' if its mean ΔBS is larger than 0 and as 'softer' if the cluster mean is negative. In addition, we validate the change detection results by comparing them with seabed changes revealed by the ground truth bottom samples collected in 2021 and 2024.

4.5.1. Area BoS

All clustering methods reveal similar spatial patterns in the change maps for Area BoS (Fig. 13). Due to the unsatisfactory clustering performance of the nadir beams, only results for incident angles between 25° and 60° are presented. The change maps from K-Means, GMM-r, and CGMM-r show a greater mixture of the three clusters compared to the other two methods, which aligns with the silhouette coefficient results (see Fig. 8 and 10).

For CGMM-r and CGMM-k, clusters 1, 2, and 3 can be interpreted as 'unchanged', 'softer', and 'coarser', respectively. Most of the western seabed of BoS is classified as 'unchanged'. Besides, a stripe pattern (Zone *S* circled in Fig. 13(e) suggests areas where the seabed may have become 'coarser' in 2024 compared to 2021. On the eastern seabed, an alternating pattern of the 'softer' and 'coarser' detections is observed.

This alternating pattern on the eastern seabed may be attributed to sediment movement over time, as indicated by the bathymetry data along four profile lines in Area BoS (Fig. 14). In 2021 and 2024, BoS exhibited similar geomorphological features, such as the bathymetric drop in the middle and the heterogeneous reef-like structures with a height of about 40 cm in the east. However, the relocation of those reef-like structures after almost three years can be noticed. Comparing the bathymetric

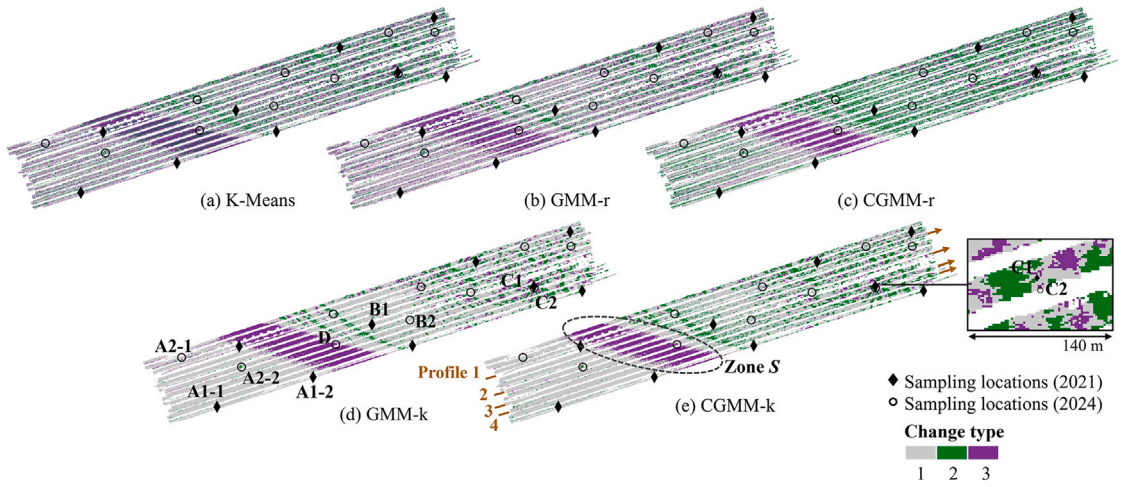

Fig. 13. 3-cluster change maps for Area BoS. Results for incident angles between 25° and 60° are presented. For the CGMM methods, the change type 1, 2, and 3 can be regarded as 'unchanged', 'softer', and 'coarser', respectively.

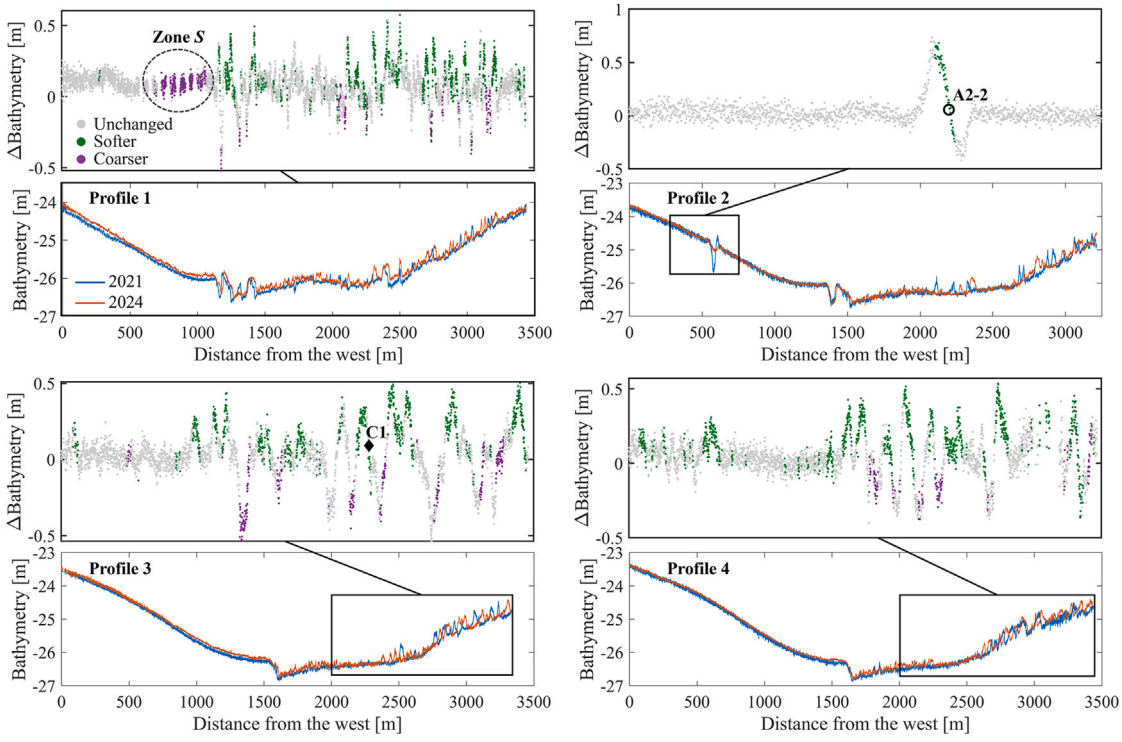

Fig. 14. Comparison of bathymetry profiles between 2021 and 2024, colored by the CGMM-k change detection results. ΔBathymetry is calculated by subtracting the bathymetry in 2021 from that measured in 2024.

difference with the CGMM-k change detection results reveals that the 'softer' and 'coarser' seabed east of the bathymetric drop corresponds to the increase and decrease in bathymetry, respectively. The consistent amplitude of these changes further supports the possibility of horizontal sediment movement (see Profile 1, 3, 4 in Fig. 14). In addition, bathymetric differences along Profile 2 also show 'softer' locations on the western seabed that might be due to sediment transport (near the sampling location A2-2). By contrast, the 'coarser' seabed in Zone *S* in the west does not experience significant changes in bathymetry.

Seabed samples collected in 2021 and 2024 also help to validate the change detection results. The Folk class, *L. conchilega* density, and dead shell content of three sample groups are compared (see Table 2). Each group includes samples taken from different years but at nearby locations. Group A (A1-1, A1-2, A2-1, and A2-2 shown in Fig. 13(d) contains sediments with the same Folk class, which aligns with the 'unchanged' seabed type indicated by the CGMM-k results. However, the average *L. conchilega* density of A2-1 and A2-2 is higher than in A1-1 and A1-2. Nevertheless, very few *L. conchilega* are found for Group A in general. The dead shell content shows a slight increase in 2024 compared to 2021. Similarly, for Group B, the Folk class remains unchanged, with a moderate increase in dead shell content. However, the *L. conchilega* density drops significantly from 2021 to 2024, which is consistent with the detected seabed change. The 'softer' detections from CGMM-k in the neighborhood of sampling locations B1 and B2 may result from the lower

Table 2
Comparison between change detection results and changes in seabed sample properties (2021 → 2024) for Area BoS.

	Group A[1]	Group B	Group C
Folk class	fS → fS	gmS → gmS	mS → cS
L. conchilega density [ind/m^2]	17.1 → 64.1	**1175.2 → 0**	653.8 → 179.5
dead shell content [%]	0.26 → 1.51	0.18 → 1.72	1.30 → 2.23
Change type predicted by CGMM-k	Unchanged	**Softer**	–

[1] Locations of samples from Group A, B, and C are shown in Fig. 13(d). For Group A, average values of samples from the same year are presented.

presence of *L. conchilega* in spring 2024, though more ground truthing is required to confirm this.

C1 and C2 are located close to each other, but in a heterogeneous region, which might explain why they lead to different seabed change types (see the zoomed-in plot in Fig. 13(e). Folk classes of C1 and C2 might show the difference in the sediment from the reef-like structures (mS) and troughs between them (cS). In addition, C1 has a much higher *L. conchilega* density than C2, possibly due to the different sediment types or seasonal variations in the abundance of *L. conchilega*. Moreover, Location D on the western seabed of BoS is classified as 'coarser' by CGMM-k, likely due to the presence of empty shells, as observed in box-core pictures and video transects for sampling locations from Group A and Location D. The seabed videos also show a brownish color of the sediment at Location D, possibly indicating organic matter left by the living shellfish. However, no 2021 samples are available in Zone *S* to validate the detected seabed change.

4.5.2. Area AT

As observed from the CGMM-r and CGMM-k change maps, the 'unchanged' detections are sparse in the northeast of Area AT (Fig. 15). Some across-track inconsistency can also be noticed in the 'unchanged' detections, possibly due to the poorer clustering performance of 20°–40° compared to 40°–60°. Nevertheless, the spatial pattern of seabed change types in Area AT is more homogeneous than that in BoS. Based on the cluster mean values of ΔBS, change types 2 and 3 can be interpreted as 'slightly softer' and 'softer', respectively. The 'softer' seabed is mainly located near the trough in the middle of the study area, with some presence in the west, while 'slightly softer' detection results align with the seabed slopes next to the trough.

Due to the homogeneity in each detected change type of AT, validation using bottom samples can be straightforward both qualitatively and quantitatively. Across all five ground truth sample groups, the Folk class remains unchanged, while the dead shell content shows a slight increase from 2021 to 2024 (see Table 3). By contrast, Groups A–D exhibit a decrease in *L. conchilega* density over the same period. The seabed near B1 and B2 is classified as 'slightly softer' by CGMM-k, corresponding to a decrease in the *L. conchilega* density of about 100 [ind/m^2]. In Groups C and D, the *L. conchilega* density drops by more than 600 [ind/m^2], which may explain their classification as 'softer'. In a similar manner, locations A1 and A2 are also identified as 'softer', with a decrease in the density reaching 200 [ind/m^2]. $\Delta BS(50°)$ for locations near Group A is about -5 dB, which is close to the boundary value between the change types 'slightly softer' and 'softer' given by CGMM-k (see Fig. 12). On the other hand, Group E is classified as 'slightly softer', but no significant change is observed from the sample properties. Since defining 'softer' and 'slightly softer' for the ground truth samples is challenging, the accuracy and F1-score for the binary 'changed' and 'unchanged' classification were calculated, demonstrating the effectiveness of the CGMM-k detection results with the metric values of 0.80 and 0.89, respectively.

Across both study areas, BoS and AT, the sediment types (Folk classes) remained consistent from 2021 to 2024. The slight increase in the dead shell content is not reflected in the change detection results. Seabed changes revealed by CGMM-k might be more related to the

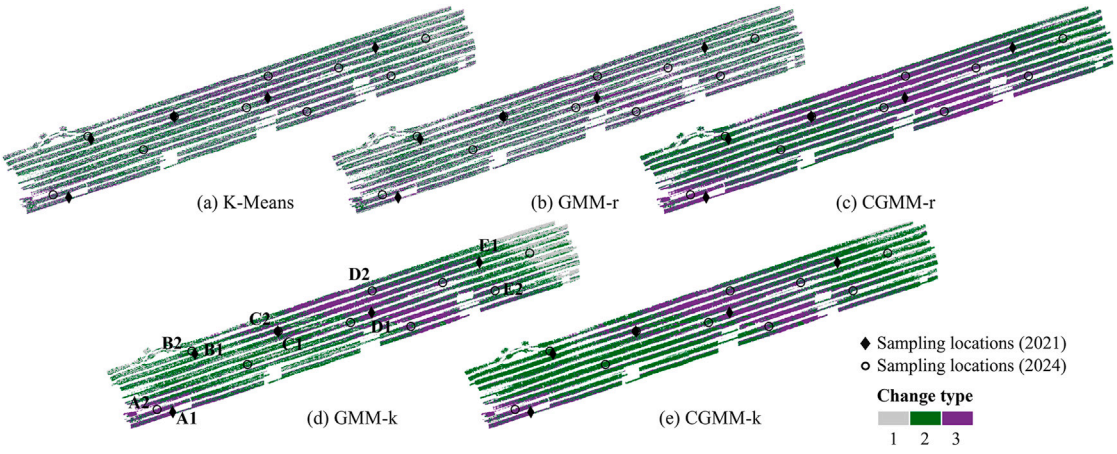

Fig. 15. 3-cluster change maps for Area AT. Results for incident angles between 25° and 60° are presented. For the CGMM methods, the change type 1, 2, and 3 can be regarded as 'unchanged', 'slightly softer', and 'softer', respectively.

Table 3
Comparison between change detection results and changes in seabed sample properties (2021 → 2024) for Area AT.

	Group A[1]	Group B	Group C	Group D	Group E
Folk class	fS → fS	fS → fS	fS → fS	mG → mG	mG → mG
L. conchilega density [ind/m^2]	**185.9 → 0**	**102.6 → 0**	**641.0 → 0**	**698.7 → 0**	12.8 → 12.8
dead shell content [%]	0.40 → 0.92	0.24 → 0.26	0.15 → 0.99	0.24 → 0.31	0.01 → 0.12
Ground truth change type	**Changed**	**Changed**	**Changed**	**Changed**	Unchanged
Change type predicted by CGMM-k	**Softer**	**Slightly softer**	**Softer**	**Softer**	Slightly softer
				Accuracy: 0.80	F1-score: 0.89

[1] Locations of samples from Group A, B, C, D, and E are indicated in Fig. 15(d).

changes in living benthos such as *L. conchilega*, which increase seabed surface roughness through their tube-building activities [43].

4.6. Limitations and future work

ΔBS between distinct surveys is affected by multiple seabed properties in a combined way. In this research, the inconsistency in sampling locations across years, especially in Area BoS, hinders the quantitative analysis of the relationships between ΔBS and various bottom properties. This also brings difficulties in validating some of our detected seabed changes. With constraints in time and budget during our surveys, priority was given to broader spatial coverage with a limited number of bottom samples. A more comprehensive study of how different seabed properties contribute to ΔBS would require long-term monitoring with consistent sampling locations. Another limitation of this research lies in the lack of an independent and long-term monitored reference area. For seabed monitoring surveys in the Dutch North Sea, well-established reference areas, such as the Kwinte area located in the Belgian North Sea [25], can be considered in the future.

In addition, this research focuses on case studies with relatively limited spatial extents in the Dutch North Sea. To investigate the influence of a wider range of seabed types and increased data volumes on BS uncertainty and change detection performance across incident angles, repeated MBES measurements in diverse seabed environments and on larger spatial scales are needed. Seabed types and ocean environments can also affect the optimal temporal interval of acoustic monitoring surveys. For the *L. conchilega* habitats investigated in this research, seasonal observations within a year might be beneficial. In sandy sediments affected by a high current speed, angular characteristics of BS measurements might change in hours due to variations in sand ripples [44], allowing for more frequent monitoring. Acoustic frequency is another key factor affecting the change detection results using ΔBS, since the relationship between BS and seabed properties is frequency dependent. BS at various frequencies can show different discrimination abilities for bottom characteristics regarding surface roughness and shallow subsurface structures. It is therefore beneficial to investigate the potential of multi-frequency backscatter for a more comprehensive seabed change analysis in the future. Moreover, based on relative calibration, future research can investigate other machine learning based benthic habitat mapping methods (e.g., [2,3,45,46]) to enhance the use of various types of acoustic features in seabed change detection.

5. Conclusion

Repeated MBES backscatter surveys can help to monitor changes in the benthic habitat, but bring the challenge of limited seabed ground truth and complexity in backscatter data processing. In this regard, we apply Gaussian Mixture Model (GMM) clustering to the backscatter difference per incident angle from repeated surveys, achieving unsupervised seabed change detection. We ensure the identification of the 'unchanged' and 'changed' seabed, by fitting the 'unchanged' cluster as a zero-mean Gaussian and constraining its variance using the estimated backscatter uncertainty from a stable reference area. The method is also flexible in describing different types of seabed changes, through fitting multiple Gaussians.

With Gaussian parameters of 'changed' clusters initialized by the K-Means clustering results, the proposed constrained GMM method shows promising change detection results for two study areas in the Dutch North Sea using 300 kHz backscatter data measured by the MBES system R2Sonic 2026. The proposed method detects the seabed change possibly caused by a reduction in the *Lanice conchilega* abundance, which might be due to seasonal changes in the seawater environment, such as temperature. For one of the study areas, the change detection results reveal alternating patterns between the seabed becoming 'coarser' and 'softer', which align with the sediment movement after almost three years, as indicated by the bathymetry data. By processing each incident angle individually, we show that backscatter data from 40° to 60° might have the greatest ability to detect seabed changes, which is consistent with the backscatter uncertainty estimation. When designing surveys for monitoring purposes, it is then helpful to increase the overlap between adjacent track lines.

Although the proposed method was tested on a specific MBES system and operating frequency in this research, it is, in principle, applicable to other systems and a broader range of frequencies, provided that appropriate relative calibration of the backscatter data is performed. Moreover, when applying the method to different seabed environments, it is essential to first investigate the relationship between backscatter measurements and seabed properties at the frequencies of interest.

Limitations of this research lie in the lack of an independent reference area and different seabed sampling locations in repeated surveys. Nevertheless, our study still demonstrates the value of using MBES backscatter data for benthic habitat monitoring, especially regarding changes in the benthic communities, which can be extended to long-term acoustic datasets in the future.

CRediT authorship contribution statement

Qian Bai: Writing – original draft, Visualization, Validation, Software, Methodology, Investigation, Formal analysis, Data curation, Conceptualization. **Alireza Amiri-Simkooei:** Writing – review & editing, Validation, Methodology, Investigation. **Sebastiaan Mestdagh:** Writing – review & editing, Validation, Investigation, Data curation. **Dick G. Simons:** Writing – review & editing, Validation, Supervision, Project administration, Funding acquisition. **Mirjam Snellen:** Writing – review & editing, Validation, Supervision, Project administration, Investigation, Funding acquisition.

Declaration of competing interest

The authors declare that they have no known competing financial interests or personal relationships that could have appeared to influence the work reported in this paper.

Acknowledgment

This study is part of the research project "Multi-spectral Multi-beam Imaging for Mapping the Occurrence of Marine Benthos" financially supported by the Dutch Research Council (NWO), with the project number 18698. The authors would like to thank the Ministry of Infrastructure and Water Management of the Netherlands (Rijkswaterstaat) for their support in survey planning and measurements onboard. Special thanks to Bureau Waardenburg and Eurofins for their help in sample collection and analyses. The company QPS is thanked for providing licenses for their software for hydrographic data collection and processing. R2Sonic and Van Oord are also acknowledged for providing sonar equipment. Finally, the authors express their gratitude to Boskalis and Deltares for their technical support.

Data availability

Data will be made available on request.

References

[1] Brown CJ, Smith SJ, Lawton P, Anderson JT. Benthic habitat mapping: a review of progress towards improved understanding of the spatial Ecology of the seafloor using acoustic techniques. Estuar Coast Shelf Sci 2011;92(3):502–20. https://doi.org/10.1016/j.ecss.2011.02.007

[2] Misiuk B, Brown CJ. Benthic habitat mapping: a review of three decades of mapping biological patterns on the seafloor. Estuar Coast Shelf Sci 2024;296:108599. https://doi.org/10.1016/j.ecss.2023.108599

[3] Loureiro G, Dias A, Almeida J, Martins A, Hong S, Silva E. A survey of seafloor characterization and mapping techniques. Remote Sens 2024;16(7):1163. https://doi.org/10.3390/rs16071163

[4] McGeady R, Runya RM, Dooley JSG, Howe JA, Fox CJ, Wheeler AJ, et al. A review of new and existing non-extractive techniques for monitoring marine protected areas. Front Mar Sci 2023;10:1126301. https://doi.org/10.3389/fmars.2023.1126301

[5] Lurton X. An introduction to underwater acoustics: principles and applications. Springer-Verlag Berlin Heidelberg; 2010. https://link.springer.com/book/9783540784807..
[6] Stephens D, Diesing M. A comparison of supervised classification methods for the prediction of substrate type using multibeam acoustic and legacy grain-size data. PLoS One 2014;9(4):e93950. https://doi.org/10.1371/journal.pone.0093950
[7] Ji X, Yang B, Tang Q. Seabed sediment classification using multibeam backscatter data based on the selecting optimal random forest model. Appl Acoust 2020;167:107387. https://doi.org/10.1016/j.apacoust.2020.107387
[8] Cui X, Liu H, Fan M, Ai B, Ma D, Yang F. Seafloor habitat mapping using multibeam bathymetric and backscatter intensity multi-features SVM classification framework. Appl Acoust 2021;174:107728. https://doi.org/10.1016/j.apacoust.2020.107728
[9] Ierodiaconou D, Monk J, Rattray A, Laurenson L, Versace VL. Comparison of automated classification techniques for predicting benthic biological communities using hydroacoustics and video observations. Cont Shelf Res 2011;31(2):S28-38. https://doi.org/10.1016/j.csr.2010.01.012
[10] Schönke M, Wiesenberg L, Schulze I, Wilken D, Darr A, Papenmeier S, et al. Impact of sparse benthic life on seafloor roughness and high-frequency acoustic scatter. Geosciences 2019;9(10):454. https://doi.org/10.3390/geosciences9100454
[11] Bai Q, Mestdagh S, Snellen M, Simons DG. Indications of marine benthos occurrence from multi-spectral multi-beam backscatter data: a case study in the North Sea. Front Earth Sci 2023;11:1140649. https://doi.org/10.3389/feart.2023.1140649
[12] Bai Q, Amiri-Simkooei A, Mestdagh S, Simons DG, Snellen M. Mussel culture monitoring with semi-supervised machine learning on multibeam echosounder data using label spreading. J Environ Manag 2024;369:122250. https://doi.org/10.1016/j.jenvman.2024.122250
[13] Menandro PS, Vieira FV, Bastos AC, Brown CJ. Exploring the multispectral acoustic response of reef habitats. Front Remote Sensin 2024;5:1490741. https://doi.org/10.3389/frsen.2024.1490741
[14] Eleftherakis D, Amiri-Simkooei A, Snellen M, Simons DG. Improving riverbed sediment classification using backscatter and depth residual features of multi-beam echo-sounder systems. J Acoust Soc Am 2012;131(5):3710–25. https://doi.org/10.1121/1.3699206
[15] Janowski L, Trzcinska K, Tegowski J, Kruss A, Rucinska-Zjadacz M, Pocwiardowski P. Nearshore benthic habitat mapping based on multi-frequency, multibeam echosounder data using a combined object-based approach: a case study from the rowy site in the southern Baltic Sea. Remote Sens 2018;10(12):1983. https://doi.org/10.3390/rs10121983
[16] Snellen M, Gaida TC, Koop L, Alevizos E, Simons DG. Performance of multibeam echosounder backscatter-based classification for monitoring sediment distributions using multitemporal large-scale ocean data sets. IEEE J Oceanic Eng 2018;44(1):142–55. https://doi.org/10.1109/JOE.2018.2791878
[17] Khelifi L, Mignotte M. Deep learning for change detection in remote sensing images: comprehensive review and meta-analysis. IEEE Access 2020;8:126385-400. https://doi.org/10.1109/ACCESS.2020.3008036
[18] Hussain M, Chen D, Cheng A, Wei H, Stanley D. Change detection from remotely sensed images: from pixel-based to object-based approaches. ISPRS J Photogramm Remote Sens 2013;80:91–106. https://doi.org/10.1016/j.isprsjprs.2013.03.006
[19] Montereale-Gavazzi G, Roche M, Lurton X, Degrendele K, Terseleer N, Van Lancker V. Seafloor change detection using multibeam echosounder backscatter: case study on the Belgian part of the North Sea. Mar Geophys Res 2018;39:229–47. https://doi.org/10.1007/s11001-017-9323-6
[20] Gaida TC, van Dijk TAGP, Snellen M, Vermaas T, Mesdag C, Simons DG. Monitoring underwater nourishments using multibeam bathymetric and backscatter time series. Coastal Eng 2020;158:103666. https://doi.org/10.1016/j.coastaleng.2020.103666
[21] Simons DG, Snellen M. A Bayesian approach to seafloor classification using multibeam echo-sounder backscatter data. Appl Acoust 2009;70(10):1258–68. https://doi.org/10.1016/j.apacoust.2008.07.013
[22] Zhang K, Lv X, Chai H, Yao J. Unsupervised SAR image change detection for few changed area based on histogram fitting error minimization. IEEE Trans Geosci Remote Sens 2022;60:1–19. https://doi.org/10.1109/TGRS.2022.3190977
[23] Schimel ACG, Ierodiaconou D, Hulands L, Kennedy DM. Accounting for uncertainty in volumes of seabed change measured with repeat multibeam sonar surveys. Cont Shelf Res 2015;111:52–68. https://doi.org/10.1016/j.csr.2015.10.019
[24] Malik M, Lurton X, Mayer L. A framework to quantify uncertainties of seafloor backscatter from swath mapping echosounders. Mar Geophys Res 2018;39:151–68. https://doi.org/10.1007/s11001-018-9346-7
[25] Roche M, Degrendele K, Vrignaud C, Loyer S, Le Bas T, Augustin JM, et al. Control of the repeatability of high frequency multibeam echosounder backscatter by using natural reference areas. Mar Geophys Res 2018;39:89–104. https://doi.org/10.1007/s11001-018-9343-x
[26] Bazi Y, Bruzzone L, Melgani F. Automatic identification of the number and values of decision thresholds in the log-ratio image for change detection in SAR images. IEEE Geosci Remote Sens Lett 2006;3(3):349–53. https://doi.org/10.1109/LGRS.2006.869973
[27] Amiri-Simkooei A, Snellen M, Simons DG. Riverbed sediment classification using multi-beam echo-sounder backscatter data. J Acoust Soc Am 2009;126(4):1724–38. https://doi.org/10.1121/1.3205397
[28] Gaida TC. Acoustic mapping and monitoring of the seabed: from single-frequency to multispectral multibeam backscatter [Ph.D. thesis]. Delft University of Technology; 2020. https://doi.org/10.4233/uuid:52b8e925-b619-45f8-9056-39454e82fe02
[29] Eleftherakis D, Berger L, Le Bouffant N, Pacault A, Augustin JM, Lurton X. Backscatter calibration of high-frequency multibeam echosounder using a reference single-beam system, on natural seafloor. Mar Geophys Res 2018;39:55–73. https://doi.org/10.1007/s11001-018-9348-5
[30] Seber GAF. Multivariate observations. John Wiley & Sons; 2009. https://www.wiley.com/en-us/Multivariate+Observations-p-9780471691211..
[31] Moon TK. The expectation-maximization algorithm. IEEE Signal Process Mag 1996;13(6):47–60. https://doi.org/10.1109/79.543975
[32] Rousseeuw PJ. Silhouettes: a graphical aid to the interpretation and validation of cluster analysis. J Comput Appl Math 1987;20:53–65. https://doi.org/10.1016/0377-0427(87)90125-7
[33] Neath AA, Cavanaugh JE. The Bayesian information criterion: background, derivation, and applications. Wiley Interdiscip Rev Comput Stat 2012;4(2):199–203. https://doi.org/10.1002/wics.199
[34] Wienhoven M, Maes J, van Doorn T, Schutte H, Salkovic K. Scenario study for the Dutch part of the North Sea. Ecorys; 2023. https://open.rijkswaterstaat.nl/zoeken/@260302/scenario-study-for-the-dutch-part-the/.
[35] Mamede da Silva Alves R. Spatial structure and temporal dynamics of an intertidal population of the marine ecosystem engineering worm lanice conchilega (Pallas, 1766) [Ph.D. thesis]. Ghent University; 2017. http://hdl.handle.net/1854/LU-8544280.
[36] Heinrich C, Feldens P, Schwarzer K. Highly dynamic biological seabed alterations revealed by side scan sonar tracking of Lanice conchilega beds offshore the island of Sylt (german bight). Geo-Mar Lett 2017;37(3):289–303. https://doi.org/10.1007/s00367-016-0477-z
[37] Callaway R. Juveniles stick to adults: recruitment of the tube-dwelling polychaete lanice conchilega (Pallas, 1766). Hydrobiologia 2003;503(1):121–30. https://doi.org/10.1023/B:HYDR.0000008494.20908.87
[38] Van Hoey G, Vincx M, Degraer S. Some recommendations for an accurate estimation of lanice conchilega density based on tube counts. Helgoland Mar Res 2006;60(4):317–21. https://doi.org/10.1007/s10152-006-0041-8
[39] Hare R. Error budget analysis for US Naval Oceanographic Office (NAVOCEANO) hydrographic survey systems. University of Southern Mississippi, Hydrographic Science Research Center for the Naval Oceanographic Office; 2001. https://www.usm.edu/hydrographic-science-research-center/publications.php.
[40] Mohammadloo TH, Snellen M, Simons DG. Assessing the performance of the multi-beam echo-sounder bathymetric uncertainty prediction model. Appl Sci 2020;10(13):4671. https://doi.org/10.3390/app10134671
[41] Roche M, Lønmo TIB, Fezzani R, Berger L, Deleu S, Bisquay H, et al. Instrumental temperature-dependence of backscatter measurements by a multibeam echosounder: findings and implications. Front Remote Sens 2025;6:1572545. https://doi.org/10.3389/frsen.2025.1572545
[42] APL. APL-UW high-frequency ocean environmental acoustic models handbook. Applied Physics Laboratory, University of Washington; 1994. https://staff.washington.edu/dushaw/epubs/APLTM9407.pdf.
[43] Schönke M, Feldens P, Wilken D, Papenmeier S, Heinrich C, von Deimling JS, et al. Impact of Lanice Conchilega on seafloor microtopography off the island of Sylt (german bight, SE North Sea). Geo-Mar Lett 2017;37:305–18. https://doi.org/10.1007/s00367-016-0491-1
[44] Koop L, van der Reijden KJ, Mestdagh S, Ysebaert T, Govers LL, Olff H, et al. Measuring centimeter-scale sand ripples using multibeam echosounder backscatter data from the Brown bank area of the Dutch Continental Shelf. Geosciences 2020;10(12):495. https://doi.org/10.3390/geosciences10120495
[45] Janowski, Wróblewski R. Application and evaluation of the AI-powered segment anything model (SAM) in seafloor mapping: a case study from Puck Lagoon, Poland. Remote Sensing 2024;16(14):2638. https://doi.org/10.3390/rs16142638
[46] Parkinson F, Douglas K, Li Z, Meijer A, Stacey CD, Kung R, et al. A generalized semiautomated method for seabed Geology classification using multibeam data and maximum likelihood classification. J Coast Res 2023;40(1):1–16. https://doi.org/10.2112/JCOASTRES-{D}-22-00095.1